

# A TDS-based approach for direct interpretation of pressure transients and fractal parameter estimation in single-porosity fractal naturally fractured reservoirs

## Abstract

This study introduces an analytical method for characterizing naturally fractured, fractal reservoirs as single-porosity systems using the Tiab Direct Synthesis (TDS) technique. By analyzing specific patterns in log-log plots of pressure and pressure derivative, such as convexity minima, slope changes, and spherical-flow behavior, direct correlations were developed to estimate the fractal dimensions ( $d_{fr}$ ,  $d_{fz}$ ) and fracture connectivity indices ( $\theta_r$ ,  $\theta_z$ ). Synthetic pressure transient responses are generated by varying key parameters of a fractal reservoir model, demonstrating how geometric and connectivity properties affect flow regimes. Normalization procedures were used to unify unique derivative behaviors, allowing the derivation of explicit analytical formulas for parameter estimation without relying on type-curve matching. The proposed correlations are validated using synthetic examples, showing strong agreement with model inputs and confirming the method's robustness. These findings suggest that the TDS technique, when adapted to fractal reservoirs, provides a rapid and reliable tool for interpreting pressure tests interpretation in heterogeneous systems.

**Keywords:** fractal reservoirs, TDS technique, well test analysis, pressure transient, single-porosity reservoirs

Volume 7 Issue 1 - 2025

Paula Sofia Sanmiguel,<sup>1</sup> Freddy Humberto Escobar,<sup>1</sup> Rodolfo Gabriel Camacho,<sup>2</sup> Juan Pablo Salazar<sup>1</sup>

<sup>1</sup>Universidad Surcolombiana, Petroleum Engineering Department, Colombia

<sup>2</sup>Universidad Nacional Autónoma de México, Petroleum Engineering Department, Mexico City

**Correspondence:** Dr. Freddy H Escobar, Petroleum Engineering Department, Universidad Surcolombiana, Colombia, Tel+57 3154195526

**Received:** November 21, 2025 | **Published:** December 09, 2025

## Nomenclature

$c_t$	Compressibility $\text{psi}^{-1}$
$C$	Wellbore storage constant, bbl/psi
$C_D$	Dimensionless wellbore storage constant
$d_{fr}$	Fractal dimension in the radial direction ( $1 \leq d_{fr} \leq 2$ )
$d_{fz}$	Fractal dimension in the vertical direction ( $0 \leq d_{fz} \leq 1$ )
$h$	Formation thickness, ft
$h_p$	Producing interval, ft
$h_{pD}$	Dimensionless producing interval
$h_{wD}$	Dimensionless depth at bottom of producing interval
$k_r$	Permeability in the radial direction, md
$k_z$	Permeability in the vertical direction, md
$k_{rw}$	Reference radial permeability at the wellbore, md
$k_{zw}$	Reference vertical permeability at the top of the anticline, md
$K\nu$	Modified Bessel function of order $\nu$
$J\nu$	Bessel function of order $\nu$
$p$	Pressure, psi
$p_i$	Initial pressure, psi
$p_{wD}$	Dimensionless wellbore pressure
$q$	Production rate, bpd
$r_w$	Wellbore radius, ft
$r_D$	Dimensionless radius
$s$	Laplace domain parameter
$S$	Mechanical skin factor
$t$	Time, hours

$t_D$	Dimensionless time
$z$	Vertical depth from the top of the dome, ft
$z_D$	Dimensionless vertical depth
$z_w$	Top position of open interval, ft
$z_{wD}$	Dimensionless depth at top of open interval
$z_{wmD}$	Dimensionless depth at medium of open interval
$t_D^{*3P}$	Dimensionless pressure derivative function, psi
$(t^* \Delta P)$	Pressure derivative function, psi

## Greek

$\phi_f$	Fracture porosity, fraction
$\mu$	Fluid viscosity, cp
$\theta_r$	Connectivity index in the radial direction ( $0 \leq \theta_r \leq 1$ )
$\theta_z$	Connectivity index in the vertical direction ( $0 \leq \theta_z \leq 1$ )

## Suffices

$D$	Dimensionless
$fr$	Fractal
$min$	Minimum
$r$	Radial
$spr$	Spherical-radial intercept

## Introduction

The dynamic characterization of naturally fractured reservoirs has long been a significant challenge in reservoir engineering because to the complex interactions among fracture networks, matrix blocks, and wellbore conditions. Early efforts to understand these systems started

in the mid-twentieth century when homogeneous, isotropic reservoir models could not fully explain classical transient pressure responses. In response to these limitations, the double-porosity/double-permeability framework was introduced, laying the foundation for interpreting the interaction between fracture storage and matrix contribution. Soon after, this theory was expanded by providing analytical solutions for systems with uniformly distributed fractures, enabling more accurate interpretation of pressure-transient data in reservoirs with significant heterogeneity.

Over the following decades, substantial progress was made in incorporating operational and wellbore-related effects into transient analysis. Studies such as those by Mavor & Cinco-Ley<sup>1</sup> and Da Prat et al.<sup>2</sup> developed corrections for wellbore storage, partial penetration, and formation damage, thereby improving the practical application of transient analysis to field conditions. At the same time, Key contributions were made by Bourdet et al.<sup>3</sup> and Tiab & Kumar<sup>4</sup> and diagnostic tools were refined introduced through the pressure derivative and improved interference testing methods. These advancements greatly improved flow-regime identification and laid the groundwork for modern diagnostic-plot analysis.

By the late twentieth century, a conceptual shift occurred with the introduction of fractal geometry to model the natural heterogeneity of fracture networks. Mandelbrot<sup>5</sup> fractal theory offered a mathematical framework capable of capturing self-similar and multiscale features of fracture systems properties that traditional Euclidean models could not adequately describe. Chang & Yortsos<sup>6</sup> first adapted fractal concepts were adapted to transient pressure analysis, demonstrating that fractal dimensions could effectively influence permeability, porosity, and connectivity distributions. Later applications by Acuna et al.<sup>7</sup> and Flamenco and Camacho<sup>8</sup> confirmed that fractal-based models could reproduce transient behaviors that were impossible to achieve with classical approaches, especially in reservoirs with substantial variability in fracture density and connectivity.

Alongside advances in reservoir modeling, Tiab<sup>8-10</sup> introduced the Tiab's Direct Synthesis (*TDS*) technique, which fundamentally transformed the approach to pressure-transient interpretation. Unlike traditional type-curve matching, used in the field, *TDS* enables direct estimation of reservoir properties from identifiable features in pressure and pressure-derivative responses. By applying precise analytical formulas instead of curve fitting, this method minimizes subjective interpretation, accelerates parameter estimation, and enhances diagnostic accuracy. Over time, the *TDS* technique has been successfully employed across various reservoir types, including homogeneous systems, dual-porosity media, horizontal wells, and hydraulically fractured wells.

Subsequent research further expanded the applicability of the *TDS* approach. Molina et al.<sup>11</sup> formulated a direct method for determining average reservoir pressure in naturally fractured systems without using type curves or correction charts, while Tiab & Bettam<sup>12</sup> extending *TDS* to hydraulically fractured wells in naturally fractured reservoirs, deriving practical expressions for fracture conductivity, permeability, and storage parameters. More recently, Jongkittinarukorn et al.<sup>13</sup> modernized *TDS* analysis for vertical wells with finite-conductivity fractures using a Laplacian analytical model. Their results demonstrated that bilinear, biradial, and radial flow regimes can be reliably detected from characteristic points in the pressure-derivative curve, affirming the versatility and robustness of *TDS* in increasingly complex scenarios.

Despite these important developments, applying *TDS* to fractal reservoir systems is still largely unexplored. Although fractal models are better at capturing multiscale heterogeneity and network connectivity than Euclidean models, there is currently no published method that combines fractal geometry with *TDS* for direct parameter estimation. This is a critical gap in the research, especially since many naturally fractured reservoirs-particularly carbonates, tight formations, and those affected by fold-and-thrust tectonics-show inherently fractal features. Properly characterizing these systems requires interpretive tools that consider scale-dependent changes in permeability and porosity, along with non-Euclidean flow behavior.

A significant antecedent in the study of naturally fractured reservoirs with multiscale heterogeneity is the work of Flamenco-López & Camacho-Velázquez<sup>14</sup> who demonstrated that fracture networks often exhibit fractal characteristics and that their transient and pseudosteady-state pressure responses follow power-law behaviors governed by fractal dimensions and connectivity indices. Their analytical and numerical results showed that fully characterizing such systems requires integrating information from both early-time and late-time flow regimes, thus highlighting the relevance of fractal parameters in interpreting pressure-transient data and motivating more direct approaches for their estimation.

The analytical framework proposed by Posadas-Mondragón & Camacho-Velázquez<sup>16</sup> offers a solid foundation for bridging this gap. Their model describes pressure transient behavior in a cylindrical single-porosity reservoir with fractal distributions of permeability and porosity in both radial and vertical directions, capturing the effects of heterogeneity and anisotropy caused by spatial variations in fracture density. Building on this framework, the present work extends the *TDS* methodology to single-porosity, naturally fractured fractal reservoirs. Synthetic pressure and derivative curves are generated using the fractal analytical model, normalized, and analyzed to identify distinctive flow features, including minima, slope transitions, and spherical-flow characteristics, unique to fractal systems. These features are used to derive direct analytical expressions for estimating key fractal parameters, including the radial and vertical fractal dimensions ( $d_{fr}, d_{fz}$ ) and fracture connectivity indices ( $\theta_r, \theta_z$ ).

The results demonstrate that the proposed methodology effectively identifies robust diagnostic signatures in the pressure derivative, enabling direct estimation of fractal parameters without relying on type-curve matching. This offers a practical and theoretically sound method for characterizing fractal reservoir systems within the *TDS* framework. By combining the benefits of fractal modeling and direct synthesis, this work provides a new and efficient tool for interpreting pressure transient tests in reservoirs where multiscale fracture networks influence fluid flow.

## Mathematical model

The mathematical model used in this study follows the one proposed by Posadas-Mondragón and Camacho-Velázquez<sup>16</sup> which considers a cylindrical reservoir with a closed boundary and single porosity. The authors incorporate fractal distributions of porosity and permeability in the radial and vertical directions, thereby representing heterogeneous, anisotropic reservoir. Based on these assumptions, the analysis is derived from the diffusivity equation expressed in cylindrical coordinates.

The fractal distribution of radial and vertical permeability is described by Equations (1) and (2) as follows:

$$k_r = k_{rw} (r / r_w)^{d_{fr} - \theta_r - D_r} \quad (1)$$

$$k_z = k_{zw}(z/r_w)^{d_{fz}-\theta_z-D_z} \quad (2)$$

The fractal dimension  $d_{fr}$  and  $d_{fz}$  indicate the fracture density in the radial and vertical directions, respectively. The connectivity indices are represented by  $\theta_r$  and  $\theta_z$ . The radial permeability formula follows the approach used by Chang and Yortsos<sup>6</sup> and Posadas-Mondragón and Camacho-Velázquez.<sup>16</sup>

Fracture porosity varies with the distance from the anticline's center and the vertical position relative to the highest point. Based on the fractal porosity distribution introduced by Cossio et al<sup>17</sup> for a two-dimensional system  $(r, z)$ , and with  $\phi_0$  representing the average porosity near the wellbore, the fracture porosity is described by Equation (3) as:

$$\phi_f = 0.5\bar{\phi}[(r/r_w)^{d_{fr}-D_r} + (z/r_w)^{d_{fz}-D_z}] \quad (3)$$

Using the following definitions for dimensionless variables:

$$r_D = r/r_w \quad (4)$$

$$z_D = z/h \quad (5)$$

$$h_D = h/r_w \quad (6)$$

$$z_D = z_w/h \quad (7)$$

$$z_{wmD} = (z_w + h_p/2)/h \quad (8)$$

$$h_{wD} = h_w/h \quad (9)$$

$$h_{pD} = h_p/h \quad (10)$$

$$\beta_r = d_{fr} - \theta_r - 1 \quad (11)$$

$$\beta_z = d_{fz} - \theta_z - 1 \quad (12)$$

$$\varepsilon = k_{zw}/k_{rw} \quad (13)$$

$$t_D = \frac{0.0002637k_{rw}t}{\phi_f \mu c_i r_w^2} \quad (14)$$

$$P_D = \frac{k_{rw} r_w (\Delta P)}{141.2q\mu B} \quad (15)$$

$$t_D * P_D' = \frac{k_{rw} h (t * \Delta P')}{141.2q\mu B} \quad (16)$$

The analytical solution in the Laplace domain, Equation (17), provided by Posadas-Mondragón & Camacho-Velázquez<sup>16</sup> is:

$$\bar{P}_{wD}(s) = \frac{2}{h_D^2 \cdot s} \sum_{n=0}^{\infty} \frac{K_{\nu_n}[\psi_n] \left\{ \frac{d_{fr}}{z_{wD}} J_{\nu_n-1} \left( a_n \frac{(z+\theta_z)}{z_{wD}} \right) - h_D^2 J_{\nu_n-1} \left( a_n h_D \frac{(z+\theta_z)}{z_{wD}} \right) \right\}}{\left[ \sqrt{s + \lambda_n} \left( \frac{1}{2} [K_{\nu_n-1}[\psi_n] + K_{\nu_n+1}[\psi_n]] - \frac{(1-\beta_r)}{2} K_{\nu_n}[\psi_n] \right) a_n^2 \left[ J_{\nu_n-1}(a_n) - \frac{\nu_n}{a_n} J_{\nu_n}(a_n) \right] \right]^2} \quad (17)$$

where  $\psi_n$  and  $a_n$  are defined as:

$$\psi_n = \left( \frac{2}{2 + \theta_r} \right) \sqrt{s + \lambda_n} \quad (18)$$

$$a_n = \frac{2}{2 + \theta_r} \sqrt{\frac{\lambda_n h_D^{2+\theta_z}}{\varepsilon}} \quad (19)$$

## Extending the TDS technique for fractal parameter estimation

According to Tiab,<sup>10</sup> the radial permeability can be estimated using Equation (20) from the pressure derivative during the radial-flow regime through:

$$k_{rw} = \frac{70.6q\mu B}{h(t * \Delta P')_r} \quad (20)$$

Additionally, the skin factor,  $s$ , can be determined using Equation (21) by selecting an arbitrary point on the radial-flow line,  $t_r$  and  $\Delta P_r$ , using:

$$s = 0.5 \left( \frac{\Delta P_r}{(t * \Delta P')_r} - \ln \left[ \frac{k t_r}{\phi_f \mu c_i r_w^2} \right] + 7.43 \right) \quad (21)$$

Figure 1 shows the dimensionless pressure derivative versus dimensionless time plotted on a log-log scale for various values of  $\theta_r$ . A distinctive behavior is observed at the point of minimum convexity.

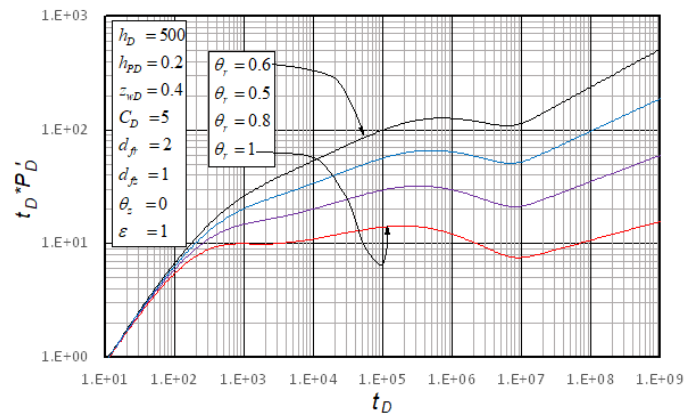


**Figure 1** Dimensionless pressure derivative versus dimensionless time log-log plot for different values of  $\theta_r$ .

To properly compare the pressure-derivative responses associated with different values of the radial connectivity index  $\theta_r$ , it was necessary to remove the scaling effects that  $\theta_r$  imposes on both the *time location* and the *magnitude* of the convexity minimum. The fractal model shows that the position of the minimum shifts systematically with  $\theta_r$  and the derivative amplitude also increases or decreases according to specific power-law relations derived from the analytical solution.

$$[(t_D * P_D') / \theta_r^3]_{\min} = 100 \quad (22)$$

For this reason, a normalization was applied to both axes of the log-log plot. The dimensionless time was multiplied by  $\theta_r^{0.7}$ , and the pressure-derivative term  $(t_D * P_D')$  was divided by  $\theta_r^3$ . These

exponents correspond to the best power-law collapse identified from the analytical behavior of Equation (17), and they effectively remove the connectivity-driven stretching of the curves. After applying these transformations, the curves corresponding to different  $\theta_r$  values collapse into a single unified trend, as shown in Figure 2. From the minimum point on the normalized curve, the relationship given by Equation (22) was obtained:

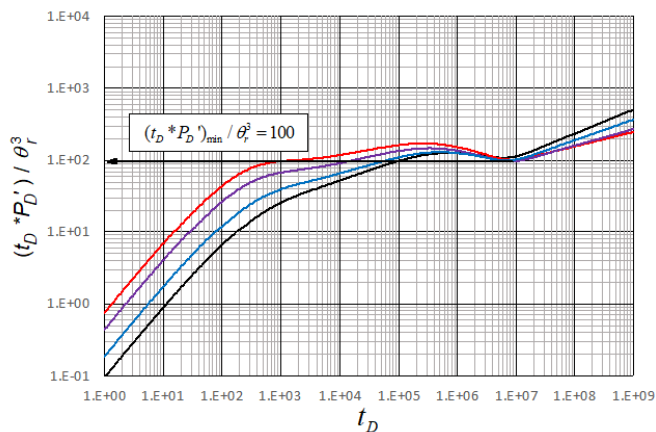


**Figure 2** Normalized dimensionless pressure derivative versus dimensionless time log-log plot for different  $\theta_r$  values.

After replacing the dimensionless pressure derivative quantity given by Equation (17), Equation (23) was found for the determination of  $\theta_r$ :

$$\theta_r = \sqrt[3]{\frac{kh(t * \Delta P')_{\min}}{14120q\mu B}} \quad (23)$$

Figure 3 shows the dimensionless pressure derivative over time for different values of  $d_{fr}$ . To compare the pressure-derivative responses obtained for different values of the radial fractal dimension  $d_{fr}$ , a normalization was required to remove the systematic stretching and amplitude changes imposed by fractal geometry. As the fractal dimension increases, the tortuosity and spatial complexity of the radial flow paths modify both the *time scale* and the magnitude of the convexity minimum in a predictable manner. These variations follow power-law trends consistent with the analytical structure of Equation (17).

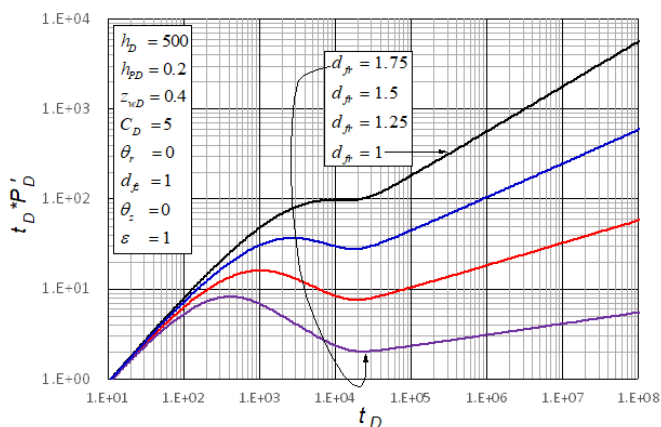


**Figure 3** Dimensionless pressure derivative versus dimensionless time log-log plot for different values of  $d_{fr}$ .

To isolate the geometric effect, the dimensionless time was multiplied by  $d_{fr}r^{1.2}$ , and the pressure-derivative term ( $t_D * P_D'$ ) was divided by  $d_{fr}^{4.5}$ . These exponents provide the best collapse of the model-generated curves and correspond to the inherent scaling imposed by the fractal permeability and porosity distributions. After applying these transformations, all curves fall on a single unified trend (Figure 4), allowing the minimum point to be uniquely identified. This minimum point led to Equation (24):

$$(t_D * P_D')e^{5.1d_{fr}} = 16968 \quad (24)$$

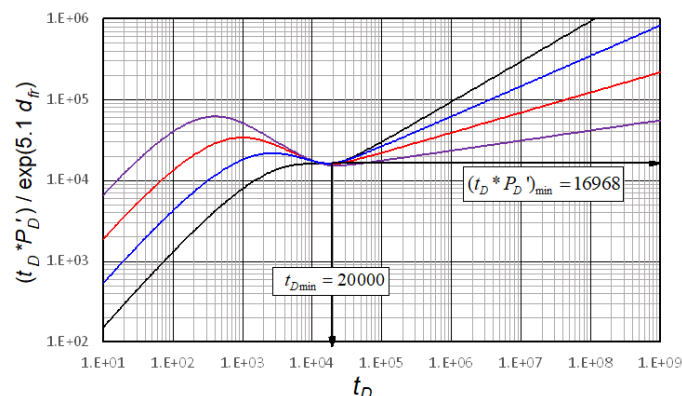


**Figure 4** Normalized dimensionless pressure derivative versus dimensionless time log-log plot for different  $d_{fr}$  values.

Substituting the dimensionless derivative from Equation (17) into Equation (23) produces the expression given by Equation (25) which is used to calculate the fractal dimension for radial connectivity.

$$d_{fr} = 14.689 + \frac{1}{5.1} \ln \left( \frac{q\mu B}{k_{rw}h(t * \Delta P')_{\min}} \right) \quad (25)$$

Figure 5 shows that the derivative slope during radial flow increases with higher  $d_{fr}$  values. Based on this trend, Equation (26) was derived:

$$d_{fr} = -2m + 2 \quad (26)$$

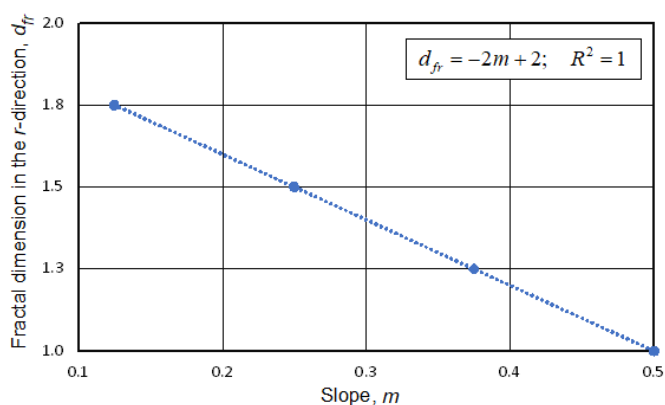


**Figure 5** Relationship between the slope of the radial flow slope of pressure derivative against  $d_{fr}$ .

The pressure derivative during radial flow exhibits zero slope but can be described by the following governing Equation (27):

$$(t * P_D')_{fr} = 0.5(t_D)_{fr}^m \quad (27)$$

Where the subscript  $fr$  denotes the fractal dimension and  $m$  is the slope of the pressure derivative during the radial flow regime. Once the dimensionless quantities given by Equations (14) and (17) are inserted into Equation (25)  $k_{rw}$  can be expressed by Equation (28) as:

$$k_{rw} = \left[ \frac{h(t^* \Delta P')_{fr}}{70.6q\mu B \left( \frac{0.0002637t_{fr}}{\phi_f \mu c_t r_w^2} \right)^m} \right]^{\frac{1}{m-1}} \quad (28)$$

Figure 6 shows the dimensionless pressure derivative versus dimensionless time plotted on a log-log scale for different values of  $\theta_z$ . The characteristic spherical-flow response is clearly identified in this figure, shifting toward later times as  $\theta_z$  increases.

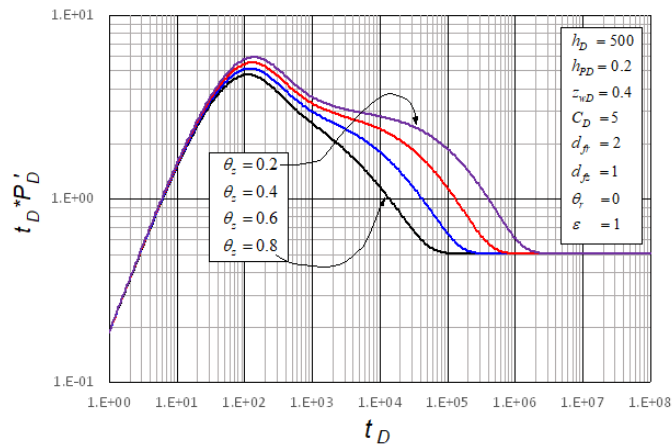


**Figure 6** Dimensionless pressure derivative versus dimensionless time log-log plot for different values of  $\theta_z$ .

The spherical-flow regime is strongly influenced by the degree of vertical connectivity within the fractured system. As the vertical connectivity index  $\theta_z$  increases, vertical diffusion becomes more efficient, causing the spherical-flow signature to appear earlier in time and modifying the curvature of the pressure-derivative response. These shifts follow an exponential trend derived from the analytical structure of Equation (17).

To remove this connectivity-driven timing distortion and to compare spherical-flow responses across different  $\theta_z$  values, the dimensionless time was multiplied by an exponential factor  $e^{5.6\theta_z}$ . This transformation collapses all spherical-flow segments onto a unified curve, as shown in Figure 7. The exponent 5.6 arises from the best-fit scaling obtained from the model-generated responses, which exhibit an exponential dependence of the spherical-flow transition time on the connectivity index. A power-law regression was applied, obtaining an analytical expression given by Equation (29) to estimate  $\theta_z$ :

$$(t_D * P'_D)_{sp} = 70 \left( \frac{(t_D)_{sp}}{\exp(5.6\theta_z)} \right)^{-0.5} \quad (29)$$

The subscript  $sp$  denotes spherical flow. By selecting an arbitrary point of time and pressure derivative during the spherical-flow period and solving for  $\theta_z$ , the expression provided by Equation (30) is obtained:

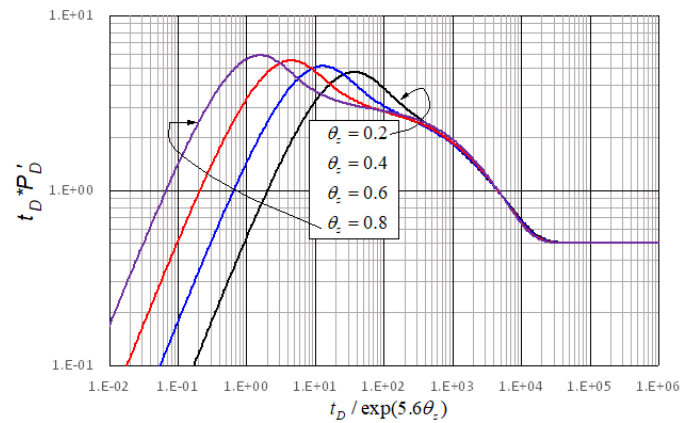


**Figure 7** Unified dimensionless pressure derivative versus dimensionless log-log plot time for different  $d_{fr}$  values.

$$\theta_z = -4.758 + \frac{1}{5.6} \ln \left( \frac{k_{rw} t_{sp}}{\phi_f \mu c_t r_w^2} \right) + \frac{2}{5.6} \ln \left( \frac{k_{rw} h(t^* \Delta P')_{sp}}{q\mu B} \right) \quad (30)$$

The intersection point between radial and spherical regimes,  $t_{spri}$ , allows the direct calculation of  $\theta_z$  as dictated by Equation (31):

$$0.5 = 70 \left( \frac{t_D}{\exp(5.6\theta_z)} \right)^{-0.5} \quad (31)$$

from which an expression to determine  $\theta_z$  was obtained once the dimensionless time, Equation (14), is plugged into Equation (30) which resulted in Equation (32),

$$\theta_z = 0.18 \ln \left( \frac{k_{rw} t_{spri}}{\phi_f \mu c_t r_w^2} \right) - 3.2626 \quad (32)$$

In Figure 8, the dimensionless pressure derivative is plotted against dimensionless time on a log-log scale for various  $d_{fe}$  values. A distinctive spherical-flow signature becomes apparent at later times as lower values are considered.

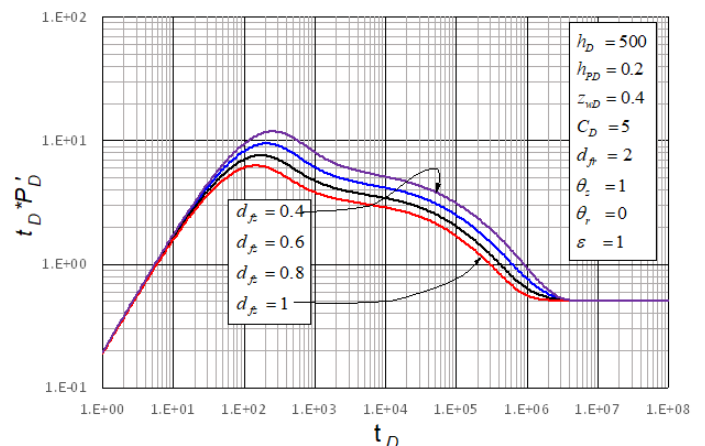


**Figure 8** Dimensionless pressure derivative versus dimensionless time behavior on a log-log plot for different values of  $d_{fe}$ .

Variations in the vertical fractal dimension  $d_{fe}$  affect the spherical-flow response by modifying the effective diffusion pathways in the

vertical direction. As  $d_{fc}$  increases, the pressure front must traverse a more tortuous and spatially complex geometry, causing a systematic delay in the onset of spherical flow as well as a reshaping of the derivative amplitude.<sup>18,19</sup>

To remove this scaling effect, the dimensionless time was multiplied by  $d_{fc} z^{1.15}$ . This exponent reflects the power-law dependence of the vertical diffusion time on the fractal geometry and provides the best curve collapse when applied to the analytical model results. After normalization, all curves converge to a unified spherical-flow profile (Figure 9), enabling the extraction of a single intercept and slope. A unified behavior given by Equation (33) was observed, yielding:

$$(t_D * P_D')_{sp} = 100[(t_D)_{sp} d_{fc}^{1.15}]^{-0.5} \quad (33)$$

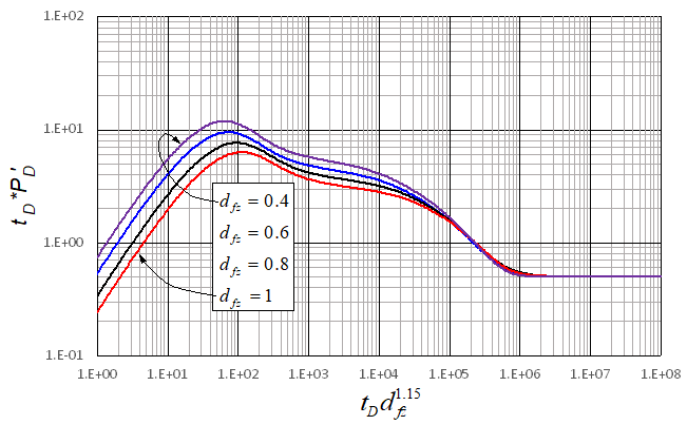


**Figure 9** Unified dimensionless pressure derivative versus dimensionless time log-log plot for different  $d_{fc}$  values.

The subscript  $sp$  also denotes spherical flow. By selecting an arbitrary point of time and pressure derivative during the spherical-flow period and solving for  $d_{fc}$ , the expression given by Equation (34) was obtained:

$$d_{fc} = 7.094 \times 10^6 \left( \frac{\phi_f \mu c_t r_w^2}{k_{rw} t_{sp}} \left[ \frac{q \mu B}{k_{rw} h (t * \Delta P')_{sp}} \right]^2 \right)^{0.869565} \quad (34)$$

Also, during radial flow, the dimensionless pressure derivative is a straight line with a slope of 0 and an intercept of 0.5. At the point where the spherical-flow line intersects with the radial-flow line, Equation (33) is set equal to 0.5 giving place to Equation (35), as follows:

$$0.5 = 100[(t_D)_{sp} d_{fc}^{1.15}]^{-0.5} \quad (35)$$

Replacing the dimensionless time, Equation (14), into Equation (35), the expression provided by Equation (6) was obtained for the determination of  $f_{dz}$ ,

$$d_{fc} = 1.755 \times 10^6 \left( \frac{\phi_f \mu c_t r_w^2}{k_{rw} t_{spri}} \right)^{0.86957} \quad (36)$$

## Simulated examples

### Synthetic example 1

Figure 10 shows the log-log plot of the pressure derivative for Example 1. The goal is to estimate the radial connectivity index  $\theta_r$  and fractal dimension  $d_{fr}$ . The following data were used:

$$\begin{aligned} q &= 500 \text{ bpd} & r_w &= 0.5 & B_o &= 1.1 \\ \text{rb/stb} & & f_f &= 0.3 & & \\ \mu &= 35 \text{ cp} & c_t &= 1 \times 10^{-5} \text{ psi}^{-1} & h &= 400 \text{ ft} \\ & & d_{fc} &= 1 & & \\ \theta_z &= 0 & \varepsilon &= 1 & & \\ z_w &= 160 \text{ ft} & h_p &= 80 \text{ ft} & & \\ & & h_w &= 240 \text{ ft} & P_i &= 3000 \text{ psi} \end{aligned}$$

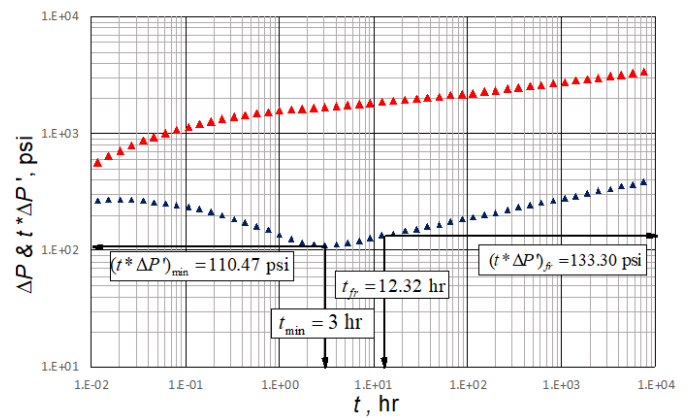


**Figure 10** Pressure derivative versus time log-log plot for example 1.

From Figure 10, the following values were read for the radial-flow regime:  $t_{fr} = 12.32 \text{ hr}$ ,  $(t * \Delta P')_{fr} = 133.30 \text{ psi}$ , and a slope of  $m = 0.167$ . Using Equation (31), the radial permeability  $k_{rw}$  was calculated:

$$k_{rw} = \left[ \frac{(400)(136.4661)}{70.6 q \mu B \left( \frac{(0.0002637)(1.000045)}{(0.3)(35)(0.00001)(0.5)^2} \right)^{0.167}} \right]^{\frac{1}{0.167-1}} = 127.32 \text{ md}$$

The minimum value  $(t * \Delta P')_{min} = 110.47 \text{ psi}$  was then used in Equation (23), yielding:

$$\theta_r = \sqrt[3]{\frac{(127.32)(400)(110.47)}{14100(500)(35)(1.1)}} = 0.274$$

Finally, the fractal dimension  $d_{fr}$  was calculated with Equation (25):

$$d_{fr} = 14.689 + \frac{1}{51} \ln \left( \frac{(500)(35)(1.1)}{(127.32)(400)(110.47)} \right) = 1.77$$

Then, the radial fractal dimension was re-calculated using Equation (26), resulting in the following value:

$$d_{fr} = -2(0.167) + 2 = 1.666$$

### Synthetic example 2

To determine the vertical connectivity ( $\theta_z$ ) and vertical fractal dimension ( $d_{fz}$ ), the pressure derivative response in Figure 11 is used along with the following data:

$q = 650$ bpd	$r_w = 0.5$	$B_o = 1.1$
rb/stb	$f_f = 0.3$	
$\mu = 18$ cp	$c_t = 1 \times 10^{-5}$ psi <sup>-1</sup>	$h = 250$ ft
	$d_{fr} = 2$	
$\theta_r = 0$	$\varepsilon = 1$	
$z_w = 100$ ft	$h_p = 50$ ft	
$h_w = 150$ ft	$P_i = 3200$ psi	

From Figure 11, the values  $(t^* \Delta P^*)_r = 10.38$  psi,  $t_{spri} = 120$  hr,  $t_{sp} = 6.33$  hr, and  $(t^* \Delta P^*)_{sp} = 50.13$  psi were read and initially used to calculate  $k_{rw}$  using Equation (20):

$$k_{rw} = \frac{70.6(650)(18)(1.1)}{250(10.38)} = 350 \text{ md}$$

The value of  $d_{fz}$  was obtained using Equation (36):

$$d_{fz} = 1.755 \times 10^6 \left( \frac{(0.3)(18)(1 \times 10^{-5})(0.5)^2}{(350)(120)} \right)^{0.86957} = 0.0098$$

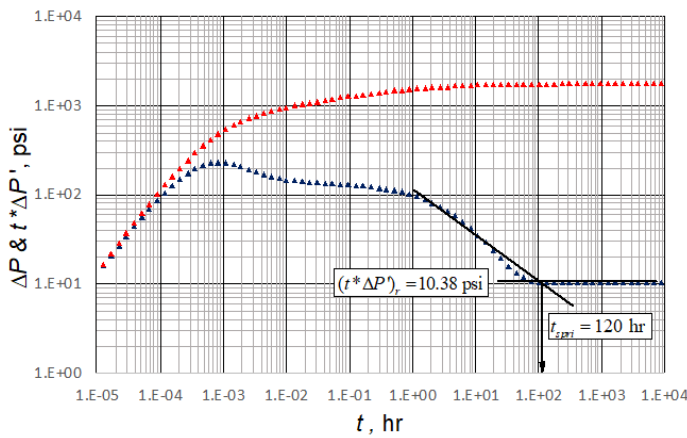


Figure 11 Pressure derivative versus time log-log plot for example 2.

This value was verified using Equation (34), and  $\theta_z$  was calculated with Equation (32). Additional verification was achieved by applying Equation (30):

$$d_{fz} = 7.094 \times 10^6 \left( \frac{(0.3)(18)(1 \times 10^{-5})(0.5)^2}{(350)(6.33)} \left( \frac{(650)(18)(1.1)}{(350)(250)(50.13)} \right)^2 \right)^{0.869565} = 0.000020866$$

$$\theta_z = 0.18 \ln \left( \frac{(350)(120)}{(0.3)(18)(1 \times 10^{-5})(0.5)^2} \right) - 3.2626 = 0.67$$

$$\theta_z = -4.758 + \frac{1}{5.6} \ln \left( \frac{(350)(6.33)}{(0.3)(18)(0.00001)(0.5)^2} \right) + \frac{2}{5.6} \ln \left( \frac{(350)(250)(50.13)}{(650)(18)(1.1)} \right) = 0.802$$

## Comments of the results

Although parameters were estimated for the synthetic examples and showed close agreement with the model inputs, a direct numerical comparison in table form was not included for an important methodological reason. The fractal parameters  $d_{fr}, d_{fz}, \theta_r, \theta_z$  exhibit the same mathematical sensitivity found in classical naturally fractured reservoirs for the storage and interporosity-flow parameters. Small changes in the location of characteristic points on the pressure-derivative curve (such as minima, inflection points, intercepts) can cause disproportionately large changes in the computed parameter values. This high sensitivity is a well-known feature of double-porosity systems and similarly affects fractal systems because of the exponential and power-law relationships in Equations (22)–(36).

Because of this sensitivity, small differences in digitization, numerical smoothing, or curve-reading resolution inevitably cause amplified deviations when calculating the fractal parameters even though the underlying analytical model remains consistent. Consequently, reporting point-by-point percentage errors between input and estimated values may give the misleading as these deviations stem from the unavoidable amplification of minor graphical errors rather than flaws in the proposed correlations.

Instead of presenting such tables, this work's validation approach emphasizes the reproducibility and stability of flow-regime behavior across a broad range of synthetic cases. The unified normalized curves (Figures 2, 4, 7, and 9) show that the analytical formulations consistently unify different responses into common trends. This unification confirms that the derived expressions accurately represent the underlying physics and the scaling behavior of fractal connectivity and geometry. The synthetic examples further demonstrate that, when characteristic points are correctly identified, the estimated parameters fall within expected ranges and reproduce the diagnostic features of the input curves.

Furthermore, a full sensitivity analysis is unnecessary because the behavior of these parameters regarding the derivative curve is already clear from the fractal diffusivity solution: each parameter causes a unique and predictable change in the log-log response. This offers an inherent qualitative sensitivity assessment.

Therefore:

$\theta_r$  and  $d_{fr}$  shift the convexity minimum and alter the radial-flow derivative level;

$\theta_z$  and  $d_{fz}$  control the timing and curvature of the spherical-flow regime;

permeability and skin remain governed by their expressions and retain their expected diagnostic signatures.

These systematic effects confirm that the proposed correlations reliably respond to physical changes in the reservoir model and do not generate spurious or unstable behavior.

In summary, although numerical tables were not included, the presented synthetic cases and unified normalized curves offer a thorough and sufficient validation of the method. The apparent sensitivity of individual numerical estimates reflects the inherent mathematical behavior of fractal systems. The overall match between analytical expressions and model-generated responses confirms the robustness, reliability, and practical utility of the proposed approach for characterizing single-porosity fractal reservoirs.

## Conclusion

This study presented an analytical method that expands the Tiab Direct Synthesis (TDS) technique to single porosity fractal reservoirs by identifying unique features in pressure and pressure derivative log–log plots. These features allowed the development of explicit correlations for estimating the essential fractal parameters

$$d_{fr}, d_{fz}, \theta_r, \text{ and } \theta_z.$$

Synthetic pressure-derivative responses verified that each fractal parameter has a clear and predictable effect on specific flow regimes, enabling the direct connection of the system's dynamic behavior to its geometric and connectivity properties.

The normalization procedures applied to the curves were crucial for consolidating different responses into unified trends. This made the analytical expressions possible and ensured parameter identifiability.

Application to synthetic examples showed that the proposed correlations accurately reproduce the diagnostic behavior of the fractal model with internal consistency and practical reliability. Overall, the adapted TDS methodology offers a quick and reliable tool for interpreting pressure-transient data in heterogeneous, naturally fractured reservoirs exhibiting fractal characteristics.

## Acknowledgements

None.

## Conflicts of interest

The authors declare that there are no conflicts of interest.

## References

1. Mavor MJ, Cinco-Ley H. Transient pressure behavior of naturally fractured reservoirs. In: *SPE California Regional Meeting*. 1979.
2. Da Prat G, Ramey HJ, Cinco-Ley H. A method to determine the permeability-thickness product for a naturally fractured reservoir. *J Pet Technol*. 1982;34(6):1364–1370.
3. Bourdet D, Ayoub JA, Pirard YM. Use of pressure derivative in well-test interpretation. *SPE Form Eval*. 1989;4(2):293–302.
4. Tiab D, Kumar A. Application of the p'D function to interference analysis. *J Pet Technol*. 1980;32(8):1465–1470.
5. Mandelbrot BB. *The Fractal Geometry of Nature*. Updated and augmented ed. WH Freeman. 1986.
6. Chang J, Yortsos YC. Pressure-transient analysis of fractal reservoirs. *SPE Form Eval*. 1990;5(1):31–38.
7. Acuna JA, Ershaghi I, Yortsos YC. Practical application of fractal pressure-transient analysis in naturally fractured reservoirs. *SPE Form Eval*. 1995;10(3):173–179.
8. Tiab D. Analysis of pressure and pressure derivative without type-curve matching—III. Vertically fractured wells in closed systems. In: *SPE Western Regional Meeting*. 1993.
9. Tiab D. Analysis of pressure and pressure derivatives without type-curve matching: I—Skin and wellbore storage. In: *SPE Production Operations Symposium*. 1993.
10. Tiab D. Analysis of pressure and pressure derivative without type-curve matching—Skin and wellbore storage. *J Pet Sci Eng*. 1995;12(3):171–181.
11. Molina M, Escobar FH, Montealegre MM, et al. Application of the TDS technique for determining the average reservoir pressure for vertical wells in naturally fractured reservoirs. *Cienc Tecnol Futuro*. 2005;3(1):45–55.
12. Tiab D, Bettam Y. Practical interpretation of pressure tests of hydraulically fractured wells in a naturally fractured reservoir. In: *Latin American & Caribbean Petroleum Engineering Conference*. 2007.
13. Jongkittinarukorn K, Escobar FH, Ramirez DM, et al. Practical interpretation of pressure tests of hydraulically fractured vertical wells with finite-conductivity in naturally fractured oil and gas formations. *J Pet Explor Prod Technol*. 2021;11(8):3277–3288.
14. Flamenco-López F, Camacho-Velázquez R. Determination of fractal parameters of fracture networks using pressure-transient data. *SPE Reservoir Evaluation & Engineering*. 2003;6(01):39–47.
15. Posadas Mondragón R, Camacho-Velázquez R. Influence and determination of mechanical skin in a reservoir with a fractal behavior. In: *SPE Latin America and Caribbean Heavy and Extra Heavy Oil Conference*. 2016.
16. Cossio M, Moridis GJ, Blasingame TA. A semi-analytic solution for flow in finite-conductivity vertical fractures using fractal theory. In: *SPE Latin America and Caribbean Petroleum Engineering Conference*. Mexico. 2012.
17. Kazemi H. Pressure transient analysis of naturally fractured reservoirs with uniform fracture distribution. *Soc Pet Eng J*. 1969;9(4):451–462.
18. Warren JE, Root PJ. The behavior of naturally fractured reservoirs. *Soc Pet Eng J*. 1963;3(3):245–255.